Power generation control of a monopile hydrostatic wind turbine using an $\mathcal{H}_\infty$ loop-shaping torque controller and an LPV pitch controller

Xin Tong and Xiaowei Zhao

***Abstract*—We transform the NREL (National Renewable Energy Laboratory) 5-MW geared equipped monopile wind turbine model into a hydrostatic wind turbine (HWT) by replacing its drivetrain with a hydrostatic transmission drivetrain. Then we design an $\mathcal{H}_\infty$ loop-shaping torque controller (to regulate the motor displacement) and a linear parameter varying (LPV) blade pitch controller for the HWT. To enhance performances of the pitch control system during the transition region around the rated wind speed, we add an anti-windup (AW) compensator to the LPV controller, which would otherwise have had undesirable system responses due to pitch saturation. The LPV AW pitch controller uses the steady rotor effective wind speed as the scheduling parameter which is estimated by LIDAR (Light Detection and Ranging) preview. The simulations based on the transformed NREL 5-MW HWT model show that our torque controller achieves very good tracking behaviour while our pitch controller (no matter with or without AW) gets much improved overall performances over a gain-scheduled PI pitch controller.**

***Index Terms*—Hydrostatic transmission, LIDAR preview, linear parameter varying control, anti-windup, $\mathcal{H}_\infty$ loop-shaping.**

I. Introduction

Wind power has been used as a clean source of renewable energy with sustainable growth in penetration and investments. To harvest more frequent and stronger winds, large wind turbines are being increasingly installed offshore, which are subjected to severe weather causing tremendous stress on the drivetrains. However, the gearbox of a conventional wind turbine drivetrain is very expensive and vulnerable, whose maintenance is difficult and expensive, particularly in the offshore case [1]. Replacing the gearbox drivetrain with a hydrostatic transmission (HST) one offers a more reliable solution. The latter has a much longer life cycle. A wind turbine with an HST drivetrain is called a hydrostatic wind turbine (HWT). Figure 1 (taken from Dutta [2]) represents a typical HST drivetrain. The rotor is directly coupled to a hydraulic pump in the nacelle, driving the high pressurised oil to operate a hydraulic motor which is coupled with a generator to produce electric power. The low pressure line transports the low pressure oil back to the pump from the motor. We consider the HST drivetrain with a fixed displacement pump and a variable displacement motor, which enables the HST to offer continuously variable transmission from the rotor/pump shaft speed to the motor/generator shaft speed. This allows the utilisation of a synchronous generator without the need for power electronics to match the grid frequency [1]. The motor & generator of the HST drivetrain can be either configured in the nacelle [2], [3] or at the tower base [4], [5]. In the present paper, we consider the former configuration, which has less operation & maintenance costs [1]. Several papers discussed the influences of different HST configurations on the turbine responses [1], [6].

X. Tong and X. Zhao (Corresponding Author) are with the School of Engineering, University of Warwick, Coventry, CV4 7AL, United Kingdom, e-mail: xin.tong@warwick.ac.uk; xiaowei.zhao@warwick.ac.uk.

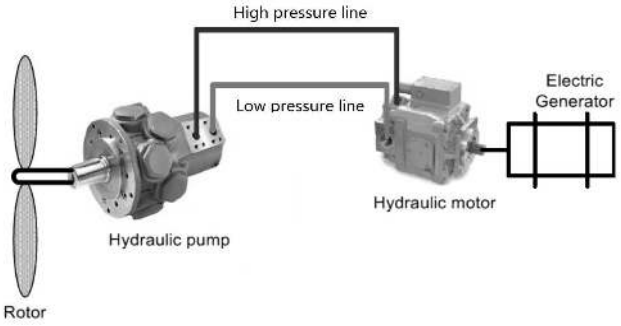

Fig. 1. Main components of a typical HST drivetrain in the HWT, as well as their connections. This figure is taken from the literature [2].

Like a conventional geared equipped variable-speed variable-pitch wind turbine, an HWT has two controllers (a torque controller and a blade pitch controller) with two main operating regions. In Region 1, the wind speed is above the cut-in value but below the rated value, where torque control takes effect to capture as much power as possible through regulating the motor displacement. In Region 2, the wind is above the rated speed, where the torque and pitch controllers work together to keep the turbine output power at its rated value and regulate the rotor speed around its rated value. Dutta employed a PI torque controller, which did not track the command well when the wind speed varied [2]. Wang and Stelson proposed a model predictive torque control scheme whose tracking performance was not desirable either [3]. Several papers designed PI/I pitch controllers based on a linearised single degree-of-freedom (DOF) model describing the angular rotation of the rotor/pump shaft [2], [4], [5]. They did not consider the undesirable responses during the transition between Regions 1 and 2 (due to pitch saturation). In addition, all the controllers introduced above were tested on simplified HWT models neglecting the tower dynamics, blade flexibility, etc. A more detailed HWT simulation model is needed to test the control design.

To solve the above challenges, we design an $\mathcal{H}_\infty$ loop-shaping torque controller and a linear parameter varying (LPV) pitch controller with an anti-windup (AW) compensator for the HWT. The LPV AW controller is scheduled by the steady rotor effective wind speed estimated by a LIDAR (Light Detection and Ranging) simulator. We assess both controllers based on a detailed aero-hydro-servo-elastic variable-speed variable-pitch HWT simulation model. This model is transformed from the well-known geared equipped NREL (National Renewable Energy Laboratory) 5-MW baseline monopile wind turbine model within FAST (Fatigue, Aerodynamics, Structures, and Turbulence), through replacing its gearbox drivetrain with an HST one as shown in Fig. 1. The simulation results demonstrate that our torque controller achieves very good tracking behaviours and our pitch controller obtains much better overall performances (in regulating the rotor speed & generator power and reducing the loads on the blade bearings & tower) than the gain-scheduled PI pitch controller developed in [5].

The structure of the paper is as follows. In Section II, we transform the NREL 5-MW geared equipped monopile wind turbine model within FAST into a detailed monopile HWT. Then in Section III, we design an $\mathcal{H}_\infty$ loop-shaping torque controller and an LPV AW blade pitch controller for the HWT. In Section IV, we test the performances of our torque and pitch controllers through simulation studies using the transformed HWT model. Finally in Section V we conclude this paper.

II. Transformation of the NREL 5-MW Baseline Monopile Wind Turbine Model within FAST into a Hydrostatic Wind Turbine

Nowadays, monopile substructures dominate offshore wind installations [7]. The NREL 5-MW baseline monopile wind turbine model represents the current typical geared equipped wind turbine [8], which is usually simulated by the NREL FAST code [9]. Its cut-in, rated, and cut-out wind speeds are 3 m/s, 11.4 m/s, and 25 m/s, respectively. In this section, we transform the NREL 5-MW baseline monopile turbine model within FAST into a detailed aero-hydro-servo-elastic hydrostatic wind turbine (HWT) model for simulation studies, by replacing its gearbox drivetrain system with the HST drivetrain shown in Fig. 1.

We employ the HST mathematical model (2.1)–(2.3) from Laguna [5], and the parameters therein which were tailored for a simplified NREL 5-MW HWT.

$$\dot{\omega}_r = \frac{1}{J_r + J_p}(\tau_{aero} - \tau_p), \tag{2.1}$$

$$\dot{D}_m = \frac{1}{T_m}(D_{md} - D_m), \tag{2.2}$$

$$\dot{\mathbf{x}}_l = \mathbf{A}_l \mathbf{x}_l + \begin{bmatrix}\mathbf{B}_{l1} & \mathbf{B}_{l2}\end{bmatrix} \begin{bmatrix}Q_p \\ Q_m\end{bmatrix}, \begin{bmatrix}P_p \\ P_m\end{bmatrix} = \begin{bmatrix}\mathbf{C}_{l1} \\ \mathbf{C}_{l2}\end{bmatrix} \mathbf{x}_l. \tag{2.3}$$

(2.1) represents the rotational motion of the rotor/pump shaft, where J_r and J_p are the moments of inertia of the rotor and pump, respectively. τ_{aero} is the aerodynamic torque which depends nonlinearly on the rotor/pump shaft speed ω_r, the rotor effective wind speed V, and the blade pitch angle β. τ_p is the pump torque described by

$$\tau_p = D_p P_p + B_p \omega_r + C_{fp} D_p P_p \tag{2.4}$$

where D_p and P_p are the pump displacement and the pressure difference across the pump, respectively. B_p and C_{fp} are the viscous damping and Coulomb friction coefficients of the pump, respectively. (2.2) describes the displacement actuator dynamics of the variable displacement motor, where D_m and D_{md} are the motor displacement and its command, respectively. T_m is the time constant. (2.3) represents the dynamics of the 10-m high pressure hydraulic line (assuming the low pressure line has constant pressure), with the flow rates of the pump and motor (Q_p and Q_m) as the inputs and the pressure differences across the pump and motor (P_p and P_m) as the outputs [5], [10]. Q_p and Q_m are given by

$$Q_p = D_p \omega_r - C_{sp} P_p,\ Q_m = D_m \omega_m + C_{sm} P_m, \tag{2.5}$$

where C_{sp} and C_{sm} are the laminar leakage coefficients of the pump and motor, respectively. ω_m is the fixed rotational speed of the assembly composed of the motor and synchronous generator. According to (2.5), Q_m varies with the change of D_m, which affects P_p in accordance with (2.3), and thus affects τ_p (2.4). The generator power is

$$p_g = \eta \tau_m \omega_m \tag{2.6}$$

where η is the generator efficiency and τ_m is the motor torque:

$$\tau_m = D_m P_m - B_m \omega_m + C_{fm} D_m P_m \tag{2.7}$$

in which B_m and C_{fm} are the viscous damping and Coulomb friction coefficients of the motor, respectively.

We modify the ElastoDyn input file of FAST (which contains the turbine structural information) to transform the gearbox drivetrain to the HST one. The relevant FAST DOFs are the generator DOF and drivetrain torsional flexibility DOF [9]. If we enable the former DOF and disable the latter one (assuming a rigid drivetrain shaft), the rotational motion of the rotor shaft is

$$\dot{\omega}_r = \frac{1}{J_r + n^2 J_g}(\tau_{aero} - n\tau_g) \tag{2.8}$$

where n is the gearbox ratio which is 97 for the baseline turbine. J_g and τ_g are the generator inertia and torque. If we set $n = 1$ and regard the generator in the geared equipped turbine as the hydraulic pump in the HWT, then (2.8) and (2.1) are equivalent. Hence, to replace the baseline rotor shaft dynamics with the HWT rotor/pump shaft dynamics, we can simply disable the drivetrain torsional flexibility DOF, set the gearbox ratio to be 1, and set the generator inertia J_g to be the pump inertia J_p in the ElastoDyn input file.

There is an interface between FAST and MATLAB/Simulink [9], through which we incorporate the mathematical model of the HST drivetrain (2.1)–(2.3) and the torque & pitch controllers (to be developed in Section III) into the NREL 5-MW wind turbine model to get an HWT.

III. Torque and Pitch Control Design of the Hydrostatic Turbine

A. Torque Control

The NREL baseline torque controller regulates the generator torque to track its command $\tau_g(\omega_{fg})$ which is inversely

proportional to the filtered generator speed ω_{fg} in Region 2 and is calculated using the $K\omega^2$ law in Region 1 [8]. The transformed NREL 5-MW hydrostatic wind turbine (HWT) employs the same torque control strategy, but the control variable becomes the pump torque. Regulation of the pump torque is typically fulfilled by adjusting the pressure difference across the pump P_p to track its command $P_{pd}(\omega_{fr})$ (where ω_{fr} is the filtered rotor speed), through controlling the motor displacement D_m. According to (2.1) and (2.8), we obtain the desired pump torque

$$\tau_{pd}(\omega_{fr}) = n\tau_g(\omega_{fg}) = n\tau_g(n\omega_{fr}) \tag{3.9}$$

where $n = 97$. Then from (2.4) we get the pressure command

$$P_{pd}(\omega_{fr}) = \frac{\tau_{pd} - B_p\omega_{fr}}{(1 + C_{fp})D_p}. \tag{3.10}$$

We design the torque controller based on the HST drivetrain model (2.1)–(2.3). The nonlinear term τ_{aero} in (2.1) depends on ω_r (rotor/pump shaft speed), V (rotor effective wind speed) and β (blade pitch angle). Therefore, we linearise the model at an operating point $(\bar{\omega}_r, \bar{V}, \bar{\beta})$ (where the bar over a variable denotes its steady value at the operating point) and derive a linear state-space model Σ_m:

$$\dot{\hat{\mathbf{x}}}_m = \mathbf{A}_m\hat{\mathbf{x}}_m + \mathbf{B}_m\hat{D}_{md} + \mathbf{B}_{md}\hat{V},\ \hat{P}_p = \mathbf{C}_m\hat{\mathbf{x}}_m, \tag{3.11}$$

in which

$$\mathbf{A}_m = \begin{bmatrix} \frac{f_{\omega_r} - B_p}{J_r + J_p} & 0 & \mathbf{A}_{13} \\ 0 & -\frac{1}{T_m} & \mathbf{0} \\ \mathbf{A}_{31} & \mathbf{A}_{32} & \mathbf{A}_{33} \end{bmatrix},\ \mathbf{B}_m = \begin{bmatrix} 0 & \frac{1}{T_m} & \mathbf{0} \end{bmatrix}^T,$$

$$\mathbf{B}_{md} = \begin{bmatrix} \frac{f_V}{J_r + J_p} & 0 & \mathbf{0} \end{bmatrix}^T,\ \mathbf{C}_m = \begin{bmatrix} 0 & 0 & \mathbf{C}_{l1} \end{bmatrix},$$

where $f_{\omega_r} = \left(\frac{\partial \tau_{aero}}{\partial \omega_r}\right)_{\bar{\omega}_r}$, $\mathbf{A}_{13} = -\frac{(D_p + C_{fp}D_p)\mathbf{C}_{l1}}{J_r + J_p}$, $\mathbf{A}_{31} = D_p\mathbf{B}_{l1}$, $\mathbf{A}_{32} = \omega_m\mathbf{B}_{l2}$, $\mathbf{A}_{33} = \mathbf{A}_l - C_{sp}\mathbf{B}_{l1}\mathbf{C}_{l1} + C_{sm}\mathbf{B}_{l2}\mathbf{C}_{l2}$ and $f_V = \left(\frac{\partial \tau_{aero}}{\partial V}\right)_{\bar{\omega}_r, \bar{V}, \bar{\beta}}$. The state variable vector is $\hat{\mathbf{x}}_m = \begin{bmatrix} \hat{\omega}_r & \hat{D}_m & \hat{\mathbf{x}}_l \end{bmatrix}^T$ where $\hat{\mathbf{x}}_m = \mathbf{x}_m - \bar{\mathbf{x}}_m$ in which $\mathbf{x}_m = \begin{bmatrix} \omega_r & D_m & \mathbf{x}_l \end{bmatrix}^T$. The input is $\hat{D}_{md} = D_{md} - \bar{D}_m$. The disturbance is $\hat{V} = V - \bar{V}$. The output is $\hat{P}_p = P_p - P_{pd}$. We choose the operating point at $\bar{V} = 9$m/s in Region 1 where the blade pitch controller does not work and $\bar{\beta} = 0°$. So in Σ_m we neglect blade pitch actuator dynamics and τ_{aero} only depends on ω_r and V. The values of f_{ω_r} and f_V are derived through FAST linearisation at the operating point [9]. We denote the transfer function from $\hat{D}_{md}$ to $\hat{P}_p$ by G_m with the state-space realisation $(\mathbf{A}_m, \mathbf{B}_m, \mathbf{C}_m, 0)$.

The highest natural frequency of the NREL 5-MW baseline monopile turbine is about 2.5 Hz [11]. Hence, we choose the number of modes for the hydraulic line to be 10, so the line's modal frequencies are in a wide range of [0, 93.12] Hz. This results in a stable 23rd-order plant G_m. We use the singular perturbation approximation method [12] to reduce the order of G_m so that the reduced model G_{rm} can match G_m well at low frequencies, which is sufficient for our control design due to slow variations of ω_{fr}. Based on the Hankel singular values of G_m in Fig. 2, we discard 14 states with relatively small singular values. We derive G_{rm} using the Matlab function

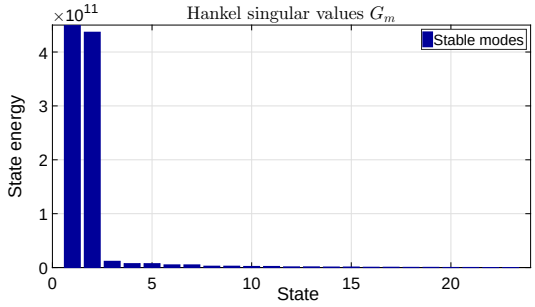

Fig. 2. Hankel singular values of the 23rd-order plant G_m.

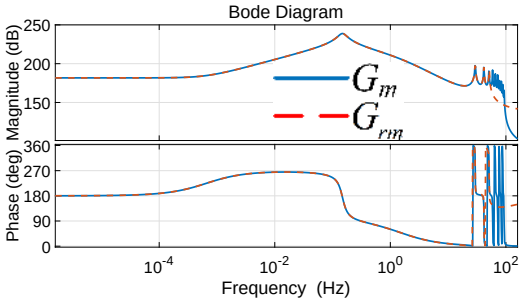

Fig. 3. Bode frequency responses of the original 23rd-order plant G_m and its reduced 9th-order model G_{rm}.

balred [13]. Fig 3 shows the Bode frequency responses of the original model G_m and the reduced-order model G_{rm}. Clearly, G_{rm} matches G_m very well at frequencies below 40 Hz.

Using the $\mathcal{H}_\infty$ loop-shaping approach [14], we design a torque controller K_m based on G_{rm} to shape the singular values of the open-loop transfer function $G_s = G_{rm}K_m$ to match closely those of a desired transfer function G_{md} and simultaneously stabilise the closed-loop system. We select

$$G_{md}(s) = \frac{930}{(s + 1e-7)(s + 50)} \tag{3.12}$$

which has high gain at low frequencies, implying low tracking error in the steady state. Its gain crossover frequency is 17.88 rad/s and the high-frequency roll-off is about -40 dB/decade, which indicates fast tracking performance and good robustness against unstructured model uncertainties. Subsequently, we derive a pre-compensator W_m such that the singular values of $G_W = G_{rm}W_m$ are identical to those of G_{md} in the frequency range $[0, \infty)$, using the algorithm proposed by Doyle [15]. The resulting closed loop is unstable because the original (uncompensated) closed-loop system has right-half-plane poles and zeros [16]. To guarantee a stabilising controller, we conduct $\mathcal{H}_\infty$ synthesis [14] by first calculating a normalised coprime factorisation of G_W:

$$G_W = M_W^{-1}N_W \tag{3.13}$$

in which $N_W N_W^* + M_W M_W^* = 1$. The perturbed system of G_W is then written as

$$\tilde{G}_W = (M_W + \Delta_1)^{-1}(N_W + \Delta_2) \tag{3.14}$$

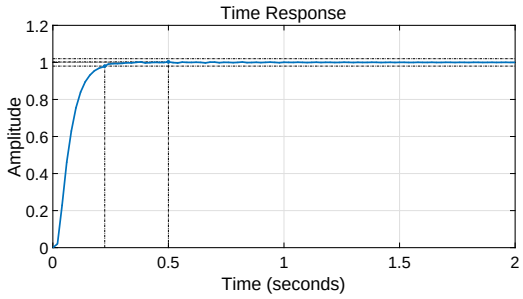

Fig. 4. Closed-loop step response.

where Δ_1, Δ_2 are stable unknown modelling uncertainties. Now consider finding an optimal $\mathcal{H}_\infty$ controller K_s to minimise ν_s such that

$$\left\| \begin{bmatrix} K_s \\ 1 \end{bmatrix} (1 - G_W K_s)^{-1} M_W^{-1} \right\|_\infty \leq \nu_s. \tag{3.15}$$

According to Lemma 3.1 in [14], K_s ensures the closed-loop stability if $\left\| \begin{bmatrix} \Delta_1 & \Delta_2 \end{bmatrix} \right\|_\infty \leq \nu_s^{-1}$. Finally, we get the torque controller:

$$K_m = W_m K_s \tag{3.16}$$

which can be solved by the Matlab function *loopsyn* [14]. The resulting closed-loop gain is $\nu_s = 1.78$, which means that the modelling uncertainties of less than 0.56 are tolerated. The phase and minimum gain margins of $G_m K_m$ are 73.4 deg and 11.3 dB, respectively. The closed-loop step response has an overshoot of 0 and a settling time of 0.22 s (see Fig. 4). These results demonstrate that the closed-loop system has good robust stability and tracking performance.

We mention that, since G_{rm} and G_{md} are stable and realizable, W_m and G_W are stable and realizable [15]. This results in a realizable K_s and thus a realizable K_m [14].

B. Pitch Control Using LIDAR Wind Preview

In Region 2, blade pitch control regulates the rotor speed around its rated value. First we design an LPV pitch controller. Then we design an AW compensator for it for the purpose of the system's recovery after pitch saturation during the transition between Regions 1 and 2. The LPV AW pitch controller uses the steady rotor effective wind speed (estimated by a LIDAR simulator) as the scheduling parameter.

1) LPV Pitch Controller: We design the pitch controller by taking the rotor/pump shaft dynamics (2.1) and the blade pitch actuator dynamics into account. The latter one is represented by a first-order time delay

$$\dot{\beta} = \frac{1}{T_\beta}(\beta_d - \beta) \tag{3.17}$$

where β and β_d are the pitch angle and its command, respectively. $T_\beta = 0.1$s is the time constant. To maintain the constant rated rotor power in Region 2, the torque controller regulates the pump torque τ_p to be inversely proportional to the rotor speed ω_r. Then (2.1) is rewritten as

$$\dot{\omega}_r = \frac{1}{J_r + J_p} \left(\tau_{aero}(\omega_r, V, \beta) - \frac{p_r}{\omega_r} \right) \tag{3.18}$$

where $p_r = 5.2966\text{e}6\,\text{W}$ is the rated rotor power. Combining (3.17) and (3.18), we derive a nonlinear model. By linearising it at an operating point $(\bar{\omega}_r, \bar{V}, \bar{\beta})$, we obtain

$$\dot{\hat{\mathbf{x}}}_p = \mathbf{A}_p \hat{\mathbf{x}}_p + \mathbf{B}_p \hat{\beta}_d + \mathbf{B}_{pd} \hat{V},\ \hat{\omega}_r = \mathbf{C}_p \hat{\mathbf{x}}_p, \tag{3.19}$$

in which

$$\mathbf{A}_p = \begin{bmatrix} \frac{f_{\omega_r} + \frac{p_r}{\bar{\omega}_r^2}}{J_r + J_p} & \frac{f_\beta}{J_r + J_p} \\ 0 & -\frac{1}{T_\beta} \end{bmatrix},\ \mathbf{B}_p = \begin{bmatrix} 0 & \frac{1}{T_\beta} \end{bmatrix}^T, \tag{3.20}$$

$$\mathbf{C}_p = \begin{bmatrix} 1 & 0 \end{bmatrix},\ \mathbf{B}_{pd} = \begin{bmatrix} \frac{f_V}{J_r + J_p} & 0 \end{bmatrix}^T, \tag{3.21}$$

where $f_\beta = \left(\frac{\partial \tau_{aero}}{\partial \beta} \right)_{\bar{\omega}_r, \bar{V}, \bar{\beta}}$. The state variable vector is $\hat{\mathbf{x}}_p = \begin{bmatrix} \hat{\omega}_r & \hat{\beta} \end{bmatrix}^T$, where $\hat{\mathbf{x}}_p = \mathbf{x}_p - \bar{\mathbf{x}}_p$ in which $\mathbf{x}_p = \begin{bmatrix} \omega_r & \beta \end{bmatrix}^T$. The input is $\hat{\beta}_d = \beta_d - \bar{\beta}$. The disturbance is $\hat{V} = V - \bar{V}$. The output is $\hat{\omega}_r = \omega_r - \bar{\omega}_r$. In Region 2, $\bar{\omega}_r = 12.1$rpm. Since the steady values $\bar{\omega}_r$ and $\bar{\beta}$ depend uniquely on $\bar{V}$ over the entire operating range of the wind turbine, we treat (3.19) as an LPV model with $\bar{V}$ as the only scheduling parameter.

The design of an LPV pitch controller is to seek a controller $K_p(\bar{V})$ scheduled by $\bar{V}$ such that for the resulting closed-loop system, the induced $\mathcal{L}_2$ norm $\|\mathcal{F}\|_{\mathcal{L}_2}$ from the external signal w to the performance output $\mathbf{z} = \begin{bmatrix} z_1 & z_2 \end{bmatrix}^T$ satisfies a performance level $\gamma > 0$, i.e.,

$$\|\mathcal{F}\|_{\mathcal{L}_2} = \sup_{\substack{w \neq 0 \\ \bar{V} \in \Theta}} \frac{\|\mathbf{z}\|_2}{\|w\|_2} < \gamma \tag{3.22}$$

in which $\|\mathbf{x}\|_2 = \sqrt{\int \mathbf{x}^T \mathbf{x} \mathrm{d}t}$ and

$$\Theta = \left\{ \sum_{j=1}^{2} \alpha_j \theta_j : \alpha_j \geq 0, \sum_{j=1}^{2} \alpha_j = 1 \right\} \tag{3.23}$$

where $\theta_1 = 11.4$ m/s and $\theta_2 = 25$ m/s are the vertices of Θ. Hence, $\bar{V} \in \Theta$ means that $\bar{V}$ varies in Region 2. The control structure is shown in Fig. 5. The external signal w is the reference value for $\hat{\omega}_r = \omega_r - \bar{\omega}_r$ which is set to be 0 to regulate the rotor speed ω_r around its rated value $\bar{\omega}_r = 12.1$rpm in Region 2. The performance output $\mathbf{z}$ is the outputs of weighting functions W_e and W_u. We select $W_e = \frac{0.5s + 0.25}{s + 5\text{e}{-4}}$, which has high gain at low frequencies to penalise the rotor speed error e and has low gain at high frequencies to limit overshoot. We select $W_u = 1.3\frac{0.1s + 0.5}{0.02s + 1}$ to limit control bandwidth and to avoid fast pitch angle variations. $G_p(\bar{V})$ has the state-space realisation $(\mathbf{A}_p, \mathbf{B}_p, \mathbf{C}_p, 0)$. $\mathbf{A}_p$ (3.20) has the nonlinear terms $f_{\omega_r}/(J_r + J_p)$ and $f_\beta/(J_r + J_p)$ which depend on $\bar{V} \in \Theta$ as shown in Fig. 6. Clearly they can be approximated by two affine functions with $\bar{V} \in \Theta$ as the independent variable. Hence, we deem $G_p(\bar{V})$ affinely dependent on $\bar{V} \in \Theta$. Note that the controller output is $\hat{\beta}_d = \beta_d - \bar{\beta}$ where $\bar{\beta}$ is a function of $\bar{V}$ (see Fig. 7). Therefore, the actual pitch angle command is $\beta_d = \hat{\beta}_d + \bar{\beta}(\bar{V})$. $\hat{\beta}_d$ is the output of the controller $K_p(\bar{V})$ as shown in Fig. 5. We obtain $\bar{\beta}(\bar{V})$ by integrating the pitch rate $\dot{\bar{\beta}}(\bar{V}) = \dot{\bar{V}} \frac{\mathrm{d}\bar{\beta}}{\mathrm{d}\bar{V}}(\bar{V})$ [17]. Such a mechanism enables us to avoid the high pitch rate near the rated wind speed 11.4 m/s as indicated in Fig. 7 (which will

$$\begin{bmatrix} \mathbf{X}\mathbf{A}(\theta_j)+\hat{\mathbf{B}}_{K_j}\mathbf{C}_2(\theta_j)+(\star) & \star & \star & \star \\ \hat{\mathbf{A}}_{K_j}^T+\mathbf{A}(\theta_j) & \mathbf{A}(\theta_j)\mathbf{Y}+\mathbf{B}_2(\theta_j)\hat{\mathbf{C}}_{K_j}+(\star) & \star & \star \\ \left[\mathbf{X}\mathbf{B}_1(\theta_j)+\hat{\mathbf{B}}_{K_j}\mathbf{D}_{21}(\theta_j)\right]^T & \mathbf{B}_1(\theta_j)^T & -\gamma\mathbf{I} & \star \\ \mathbf{C}_1(\theta_j) & \mathbf{C}_1(\theta_j)\mathbf{Y}+\mathbf{D}_{12}(\theta_j)\hat{\mathbf{C}}_{K_j} & \mathbf{D}_{11}(\theta_j) & -\gamma\mathbf{I} \end{bmatrix} < 0 \tag{3.28}$$

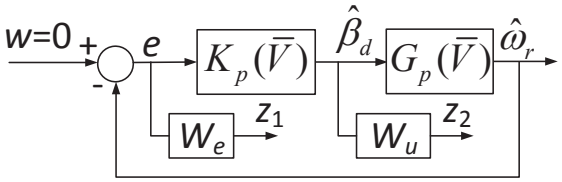

Fig. 5. Control structure of the LPV blade pitch controller $K_p(\bar{V})$.

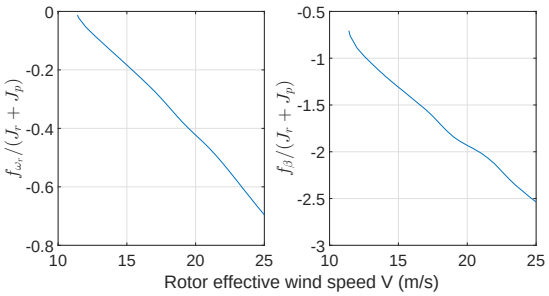

Fig. 6. $f_{\omega_r}/(J_r+J_p)$ and $f_\beta/(J_r+J_p)$ at $\bar{V}\in\Theta$.

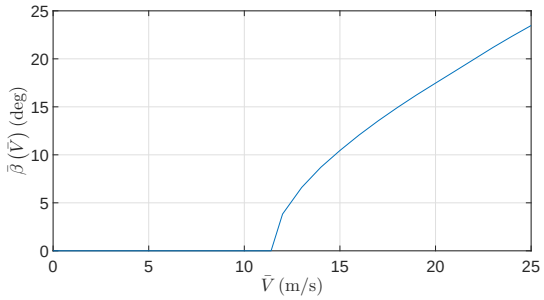

Fig. 7. Steady pitch angle $\bar{\beta}(\bar{V})$ ($\bar{V}$ is the steady rotor effective wind speed).

induce significant tower loads during the transition between Regions 1 and 2), through limiting $\mathrm{d}\bar{\beta}/\mathrm{d}\bar{V}$ to 2.5°s/m.

Following the control structure shown in Fig. 5, we obtain an augmented open-loop LPV system P_Σ:

$$\dot{\mathbf{x}} = \mathbf{A}(\bar{V})\mathbf{x}+\mathbf{B}_1(\bar{V})w+\mathbf{B}_2(\bar{V})\hat{\beta}_d, \tag{3.24}$$

$$\mathbf{z} = \mathbf{C}_1(\bar{V})\mathbf{x}+\mathbf{D}_{11}(\bar{V})w+\mathbf{D}_{12}(\bar{V})\hat{\beta}_d, \tag{3.25}$$

$$\hat{\omega}_r = \mathbf{C}_2(\bar{V})\mathbf{x}+\mathbf{D}_{21}(\bar{V})w. \tag{3.26}$$

Now we determine a stabilising LPV controller $K_p(\bar{V})$ to satisfy (3.22). Recall that $G_p(\bar{V})$ depends affinely on $\bar{V}\in\Theta$, so does its augmented system P_Σ. Hence, according to [18], first we solve an optimisation problem offline: minimising $\gamma\left(\mathbf{X},\mathbf{Y},\hat{\mathbf{A}}_{K_j},\hat{\mathbf{B}}_{K_j},\hat{\mathbf{C}}_{K_j}\right)$ $(j=1,2)$ subject to (3.27) and

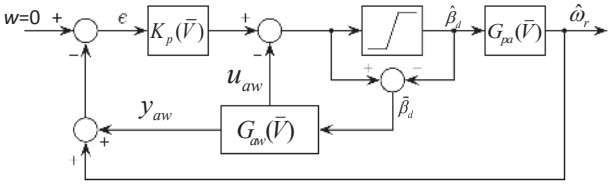

Fig. 8. Anti-windup compensation scheme for the LPV pitch controller.

(3.28) with $\star$ induced by symmetry.

$$\begin{bmatrix} \mathbf{X} & \mathbf{I} \\ \mathbf{I} & \mathbf{Y} \end{bmatrix} > 0, \mathbf{X}=\mathbf{X}^T>0, \mathbf{Y}=\mathbf{Y}^T>0 \tag{3.27}$$

Then we derive the controller K_j at the vertex θ_j with the state-space realisation $\left(\mathbf{A}_{K_j},\mathbf{B}_{K_j},\mathbf{C}_{K_j},0\right)$ in which

$$\mathbf{A}_{K_j} = \mathbf{N}_p^{-1}\Big(\hat{\mathbf{A}}_{K_j}-\mathbf{X}\mathbf{A}(\theta_j)\mathbf{Y}-\hat{\mathbf{B}}_{K_j}\mathbf{C}_2(\theta_j)\mathbf{Y} -\mathbf{X}\mathbf{B}_2(\theta_j)\hat{\mathbf{C}}_{K_j}\Big)\mathbf{M}_p^{-T}, \tag{3.29}$$

$$\mathbf{B}_{K_j} = \mathbf{N}_p^{-1}\hat{\mathbf{B}}_{K_j}, \mathbf{C}_{K_j} = \hat{\mathbf{C}}_{K_j}\mathbf{M}_p^{-T}, \tag{3.30}$$

where $\mathbf{N}_p$ and $\mathbf{M}_p$ are the solutions of the factorisation problem $\mathbf{I}-\mathbf{X}\mathbf{Y}=\mathbf{N}_p\mathbf{M}_p^T$. For the online implementation, we measure $\bar{V}$ and finally obtain the LPV pitch controller $K_p(\bar{V})$ with the state-space realisation $(\mathbf{A}_K,\mathbf{B}_K,\mathbf{C}_K,0)$ where

$$\begin{bmatrix} \mathbf{A}_K & \mathbf{B}_K \\ \mathbf{C}_K & 0 \end{bmatrix}(\bar{V}) = \sum_{j=1}^{2}\alpha_j\begin{bmatrix} \mathbf{A}_{K_j} & \mathbf{B}_{K_j} \\ \mathbf{C}_{K_j} & 0 \end{bmatrix} \tag{3.31}$$

in which $\alpha_1=\frac{25-\bar{V}}{13.6}$ and $\alpha_2=\frac{\bar{V}-11.4}{13.6}$. We mention that α_1 and α_2 can be any continuous functions of $\bar{V}$ satisfying (3.23).

2) AW Compensator: We employ the AW compensation scheme proposed in [19] for the LPV pitch controller (see Fig. 8). We mention that this AW setup can be incorporated with other pitch controllers because it is designed independently. This AW scheme is applicable only when the open-loop LPV plant is exponentially stable. However, due to the negative damping introduced by torque control (indicated by the term $p_r/\bar{\omega}_r^2$ in (3.20)), the LPV model $G_p(\bar{V})$ used for pitch control design is unstable when $\bar{V}$ is above and near the rated value 11.4 m/s. In order to obtain an exponentially stable LPV plant for the AW design, we neglect this negative damping. Such a treatment (also used in [8], [20]) means that in (3.18) the rotor reaction torque p_r/ω_r is assumed to remain at its constant steady value in Region 2. As a result, the LPV model $G_{pa}(\bar{V})$ used for the AW design is the same as $G_p(\bar{V})$ with $\mathbf{A}_p$ in (3.20) replaced with

$$\mathbf{A}_{pa} = \begin{bmatrix} \frac{f_{\omega_r}}{J_r+J_p} & \frac{f_\beta}{J_r+J_p} \\ 0 & -\frac{1}{T_\beta} \end{bmatrix}. \tag{3.32}$$

As shown in Fig. 8, the AW compensator provides two compensation terms u_{aw} and y_{aw} to the controller output and input, respectively. We define the transfer function matrix $\mathbf{G}_{aw}(\bar{V})$ of the compensator as $\mathbf{G}_{aw}(\bar{V}) = \begin{bmatrix} M(\bar{V}) - 1 & N(\bar{V}) \end{bmatrix}^T$, where $N(\bar{V})$ and $M(\bar{V})$ are the stable proper coprime transfer functions satisfying $G_{pa}(\bar{V}) = N(\bar{V})M(\bar{V})^{-1}$. Then its state-space realisation is

$$\mathbf{G}_{aw}(\bar{V}) \stackrel{s}{=} \left[\begin{array}{c|c} \mathbf{A}_{pa}(\bar{V}) + \mathbf{B}_p\mathbf{F}(\bar{V}) & \mathbf{B}_p \\ \hline \mathbf{F}(V) & 0 \\ \mathbf{C}_p & 0 \end{array}\right] \tag{3.33}$$

where $\mathbf{F}(\bar{V})$ is a state-feedback gain. To ensure quadratic stability of the closed-loop system during saturation and to minimise the effect of y_{aw} on the controller input e, the following condition is required:

$$\left\|M(\bar{V}) - 1\right\|_{\mathcal{L}_2} < 1, \left\|N(\bar{V})\right\|_{\mathcal{L}_2} < \mu, \tag{3.34}$$

which is equivalent to $\|\mathbf{G}_{aw}\|_{\mathcal{L}_2} < \mu$ with $\mu \leq 1$. To fulfil this condition, we first solve an optimisation problem offline: minimising $\mu\,(\mathbf{Q}, \mathbf{H}_j)\,(j = 1, 2)$ subject to

$$\begin{bmatrix} \mathbf{A}_{pa}(\theta_j)\mathbf{Q} + \mathbf{B}_p\mathbf{H}_j + (\star) & \star & \star & \star \\ \mathbf{B}_p^T & -\mu & \star & \star \\ \mathbf{H}_j & 0 & -\mu & \star \\ \mathbf{C}_p\mathbf{Q} & 0 & 0 & -\mu \end{bmatrix} < 0,$$
$$\mathbf{Q} = \mathbf{Q}^T > 0, \mu \leq 1. \tag{3.35}$$

Then we obtain $\mathbf{F}(\bar{V})$ at the vertex θ_j: $\mathbf{F}(\theta_j) = \mathbf{H}_j\mathbf{Q}^{-1}$. We measure $\bar{V}(t)$ online and the resulting AW compensator is

$$\mathbf{G}_{aw}(\bar{V}) \stackrel{s}{=} \sum_{j=1}^{2} \alpha_j \left[\begin{array}{c|c} \mathbf{A}_{pa}(\theta_j) + \mathbf{B}_p\mathbf{F}(\theta_j) & \mathbf{B}_p \\ \hline \mathbf{F}(\theta_j) & 0 \\ \mathbf{C}_p & 0 \end{array}\right]. \tag{3.36}$$

We use the optimisation tools Sedumi [21] and YALMIP [22] to solve the optimisation problems. Then we derive the LPV pitch controller and its AW compensator. Although they are designed for the case that the scheduling parameter $\bar{V}$ varies in Region 2, they actually work effectively in the entire operating range of the HWT. When $\bar{V}$ falls outside Region 2, they choose the state-space data at either the vertex θ_1 or θ_2 whichever is closer to $\bar{V}$. We mention that $\bar{V}$ is estimated by a nacelle-based pulsed LIDAR simulator developed by us following Schipf et. al [17].

IV. Simulation Study

In this section we test the performances of our $\mathcal{H}_\infty$ loop-shaping torque controller and LPV (with/without AW) pitch controller developed in Section III through simulation studies based on the transformed hydrostatic wind turbine (HWT) model developed in Section II. We will compare the performances of our pitch controller with a gain-scheduled PI pitch controller developed by Laguna [5] (tuned for a simplified NREL 5-MW HWT) whose proportional and integral terms K_P and K_I are:

$$K_P(\beta) = -\frac{1.6167}{1 + \frac{\beta}{6.302336}}, K_I(\beta) = -\frac{0.6929}{1 + \frac{\beta}{6.302336}}. \tag{4.37}$$

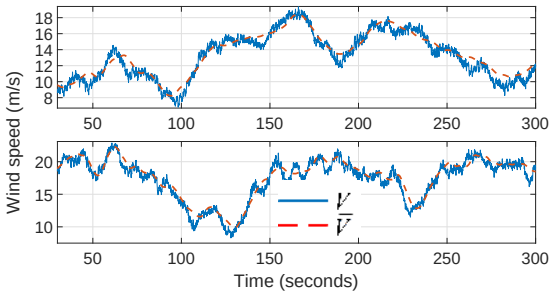

Fig. 9. Actual and estimated (by LIDAR) rotor effective wind speeds (V and $\bar{V}$) under the turbulent wind input with a mean speed of 11.4 m/s (top) or 18 m/s (bottom) along with a wave input.

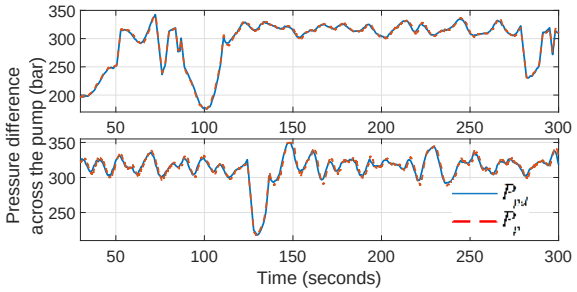

Fig. 10. Pressure command P_{pd} and actual pressure difference across the pump P_p under the turbulent wind input with a mean speed of 11.4 m/s (top) or 18 m/s (bottom) along with a wave input.

We also design a back-calculation AW compensator [23] for the above PI controller. The back-calculation coefficient is tuned to be 0.5.

We use two IEC full-field turbulent wind inputs together with a same irregular wave input during the simulations. The wind inputs are generated by NREL TurbSim [24] using the Class I Extreme Turbulence Model (ETM) with mean speeds of 11.4 m/s (rated speed) and 18 m/s, respectively. The waves are irregularly generated based on the JONSWAP/Pierson-Moskowitz spectrum by the HydroDyn module of FAST. The peak-spectral period and significant wave height of the incident waves are 10 seconds and 6 m, respectively.

Fig. 9 shows the actual rotor effective wind speed V (computed by FAST AeroDyn) and its estimation $\bar{V}$ (by LIDAR). Clearly, the correlation between these two signals at low frequencies is good. This is very desirable since the low-frequency components contain the most wind power and affect the turbine most [25]. Besides, under either wind input, V covers both Regions 1 and 2 as shown in Fig. 9. Fig. 10 shows that our $\mathcal{H}_\infty$ loop-shaping torque controller tracks the pressure command P_{pd} (3.10) effectively. The LPV AW controller is used for pitch control here.

Tables I and II list the performances of 4 different pitch controllers under the two wind inputs respectively, along with the same wave input. The same $\mathcal{H}_\infty$ loop-shaping torque controller is used for these 4 cases. Here we use the standard deviation of the collective pitch rate to evaluate the damage on the blade bearings due to pitch activity [26]. We compute the fore-aft and side-to-side damage equivalent loads (DEQLs) at

TABLE I
PERFORMANCES OF 4 PITCH CONTROLLERS UNDER THE TURBULENT WIND INPUT WITH A MEAN SPEED OF 11.4 M/S ALONG WITH A WAVE INPUT. CHANGES W.R.T. THE PI CASE ARE GIVEN IN THE BRACKETS.

	PI	LPV	LPV AW	PI AW
Average power (kW)	4309.8	4398.0 (2.05%)	4373.0 (1.47%)	4331.8 (0.51%)
Standard deviation of power (kW)	750.34	697.93 (-6.98%)	695.45 (-7.32%)	724.94 (-3.39%)
Standard deviation of pitch rate (deg)	1.20	0.61 (-49.17%)	0.74 (-38.33%)	0.88 (-26.67%)
Fore-aft DEQL (kN·m)	20614	7854.0 (-59.11%)	6197.7 (-69.93%)	7772.6 (-62.29%)
Side-to-side DEQL (kN·m)	5941.1	2338.2 (-60.64%)	2064.4 (-65.25%)	2836.3 (-52.26%)

TABLE II
PERFORMANCES OF 4 PITCH CONTROLLERS UNDER THE TURBULENT WIND INPUT WITH A MEAN SPEED OF 18 M/S ALONG WITH A WAVE INPUT. CHANGES W.R.T. THE PI CASE ARE GIVEN IN THE BRACKETS.

	PI	LPV	LPV AW	PI AW
Average power (kW)	4625.0	4681.1 (1.21%)	4679.8 (1.18%)	4628.1 (0.067%)
Standard deviation of power (kW)	393.73	288.33 (-26.77%)	287.38 (-27.01%)	369.79 (-6.08%)
Standard deviation of pitch rate (deg)	1.11	0.79 (-28.83%)	0.81 (-27.03%)	0.99 (-10.81%)
Fore-aft DEQL (kN·m)	15872	8074.8 (-49.13%)	8007.1 (-49.55%)	9392.0 (-40.83%)
Side-to-side DEQL (kN·m)	5764.0	4336.1 (-24.77%)	4173.7 (-27.59%)	5748.7 (-0.27%)

the monopile base using the NREL MLife code [27] based on the time-series of the monopile base fore-aft and side-to-side moments. As indicated in Tables I & II, our PI AW controller and LPV controllers (with and without AW) attain much better overall performances than the PI controller developed by Laguna [5] under either wind input along with the wave input, including increased average power, improved regulation of the rotor speed & generator power, and considerably reduced damage on the blade bearings & monopile tower. Considering the two cases with AW, the LPV AW controller is superior to the PI AW one especially in terms of mitigating the loads on the blade bearings & monopile tower. Fig. 11 shows the simulation results for the cases using three types of pitch controllers under the turbulent wind input with a mean speed of 11.4 m/s along with the wave input, which further verifies the conclusions from Table I. In addition, it is noticeable from Fig. 11 that significant rotor speed, generator power and tower loading variations occur due to pitch saturation during the transitions at about 55 s and 110 s (see the top diagram of Fig. 9) for the cases using the PI and LPV (without AW) controllers, while the LPV AW pitch controller achieves much smoother responses. We mention that similar phenomena are found under the turbulent wind input with a mean speed of 18 m/s along with the wave input. To avoid overlap, we only give the plot of the rotor speed responses for the cases using

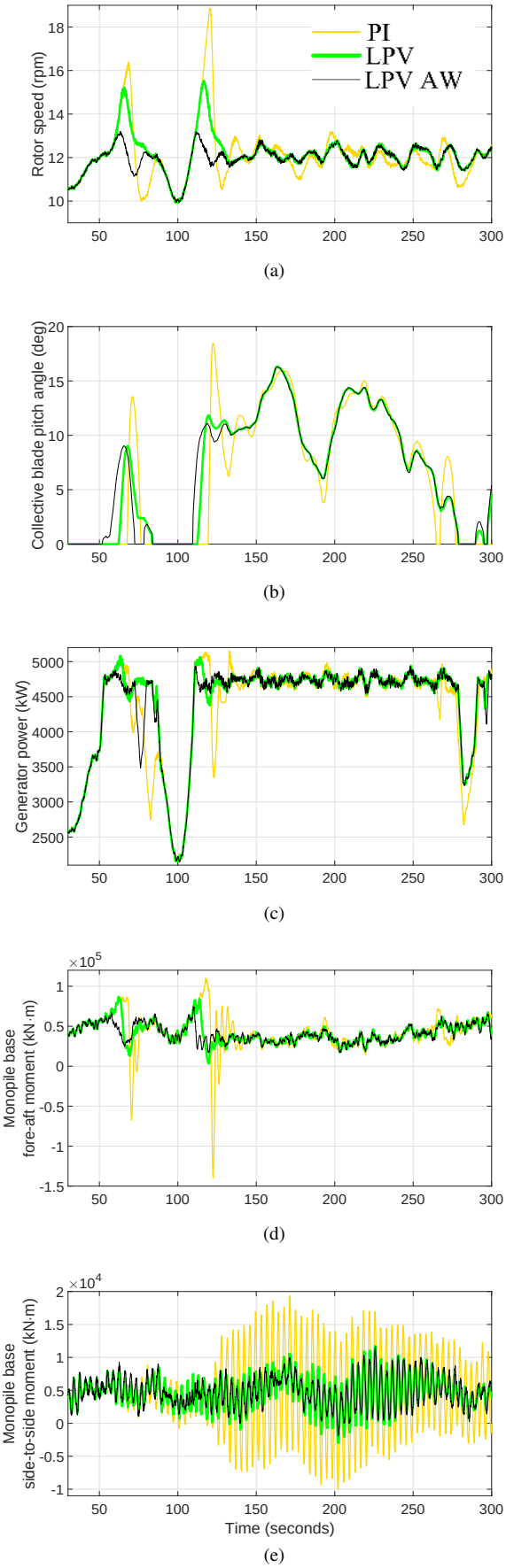

Fig. 11. Simulation results under the turbulent wind input with a mean speed of 11.4 m/s along with a wave input.

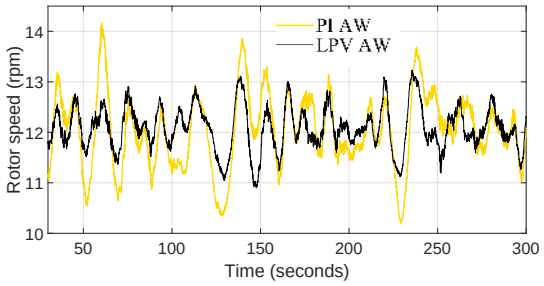

Fig. 12. Rotor speed responses under the turbulent wind input with a mean speed of 18 m/s along with a wave input.

the PI AW and LPV AW controllers in Fig. 12 where the LPV AW controller regulates the rotor speed much more tightly than its PI AW counterpart.

V. Conclusions

We transformed the NREL 5-MW geared equipped monopile wind turbine model within FAST into a detailed aero-hydro-servo-elastic hydrostatic wind turbine simulation model. We then designed an $\mathcal{H}_\infty$ loop-shaping torque controller and a LIDAR-based LPV AW pitch controller. The simulation results showed good tracking behaviours achieved by our torque controller and much improved overall performances attained by our LPV (with or without AW) pitch control scheme compared with a gain-scheduled PI pitch control system developed by Laguna [5], in terms of rotor speed regulation, power quality, and load reductions of the blade bearings & monopile tower.

One of the future directions is to develop a more detailed HST drivetrain system which incorporates the dynamics of auxiliary hydraulic components (e.g., the charging system, pressure relief valves, accumulators, and flow control valves).

References

[1] J.-C. Ossyra, "Reliable, lightweight transmissions for off-shore, utility scale wind turbines," Eaton Corporation, WI, USA, Tech. Rep., 2012.
[2] R. Dutta, "Modeling and analysis of short term energy storage for mid-size hydrostatic wind turbine," Master's thesis, Uni. of Minnesota, 2012.
[3] F. Wang and K. A. Stelson, "Model predictive control for power optimization in a hydrostatic wind turbine," in *13th Scandinavian International Conference on Fluid Power*, Sweden, Jun 2013.
[4] B. Skaare, B. Hörnsten, and F. G. Nielsen, "Modeling, simulation and control of a wind turbine with a hydraulic transmission system," *Wind Energy*, vol. 16, no. 8, pp. 1259–1276, 2013.
[5] A. J. Laguna, "Modeling and analysis of an offshore wind turbine with fluid power transmission for centralized electricity generation," *Journal of Computational and Nonlinear Dynamics*, vol. 10, p. 041002, 2015.
[6] A. J. Laguna, N. F. Diepeveen, and J. W. Van Wingerden, "Analysis of dynamics of fluid power drive-trains for variable speed wind turbines: parameter study," *IET Renewable Power Generation*, vol. 8, no. 4, pp. 398–410, 2014.
[7] X. Tong, X. Zhao, and S. Zhao, "Load reduction of a monopile wind turbine tower using optimal tuned mass dampers," *International Journal of Control*, vol. 90, no. 7, pp. 1283–1298, 2017.
[8] J. Jonkman, S. Butterfield, W. Musial, and G. Scott, "Definition of a 5-MW reference wind turbine for offshore system development," National Renewable Energy Laboratory (NREL), CO, USA, Tech. Rep., 2009.
[9] J. M. Jonkman and M. L. Buhl Jr, "FAST users guide," National Renewable Energy Laboratory (NREL), CO, USA, Tech. Rep., 2005.
[10] J. Makinen, R. Piche, and A. Ellman, "Fluid transmission line modeling using a variational method," *Journal of dynamic systems, measurement, and control*, vol. 122, no. 1, pp. 153–162, 2000.
[11] P. Passon, M. Kühn, S. Butterfield, J. Jonkman, T. Camp, and T. J. Larsen, "OC3—benchmark exercise of aero-elastic offshore wind turbine codes," in *EAWE Special Topic Conference: The Science of Making Torque from Wind*, Lyngby, Denmark, Aug. 2007.
[12] Y. Liu and B. D. Anderson, "Singular perturbation approximation of balanced systems," *International Journal of Control*, vol. 50, no. 4, pp. 1379–1405, 1989.
[13] A. Varga, "Balancing free square-root algorithm for computing singular perturbation approximations," in *30th IEEE Conference on Decision and Control*, Brighton, UK, December 1991.
[14] K. Glover and D. McFarlane, "Robust stabilization of normalized coprime factor plant descriptions with $\mathcal{H}_\infty$-bounded uncertainty," *IEEE Transactions on Automatic Control*, vol. 34, no. 8, pp. 821–830, 1989.
[15] J. Doyle, "Advances in multivariable control," Lecture Notes at ONR/Honeywell Workshop, MN, USA, October 1984.
[16] D. McFarlane and K. Glover, "A loop-shaping design procedure using $\mathcal{H}_\infty$ synthesis," *IEEE Transactions on Automatic Control*, vol. 37, no. 6, pp. 759–769, 1992.
[17] D. Schipf, E. Simley, F. Lemmer, L. Y. Pao, and P. W. Cheng, "Collective pitch feedforward control of floating wind turbines using lidar," *Journal of Ocean and Wind Energy*, vol. 2, no. 4, pp. 223–230, 2015.
[18] P. Apkarian and R. J. Adams, "Advanced gain-scheduling techniques for uncertain systems," *IEEE Transactions on control systems technology*, vol. 6, no. 1, pp. 21–32, 1998.
[19] M. C. Turner and I. Postlethwaite, "A new perspective on static and low order anti-windup synthesis," *International Journal of Control*, vol. 77, no. 1, pp. 27–44, 2004.
[20] M. H. Hansen, A. D. Hansen, T. J. Larsen, S. Øye, P. Sørensen, and P. Fuglsang, "Control design for a pitch-regulated, variable speed wind turbine," Risø National Laboratory, Denmark, Tech. Rep., 2005.
[21] J. F. Sturm, "Using SeDuMi 1.02, a MATLAB toolbox for optimization over symmetric cones," *Optimization methods and software*, vol. 11, no. 1-4, pp. 625–653, 1999.
[22] J. Lofberg, "YALMIP: A toolbox for modeling and optimization in MATLAB," in *13th IEEE International Symposium on Computer Aided Control System Design*, Taipei, Taiwan, September 2004, pp. 284–289.
[23] A. Izadbakhsh, A. A. Kalat, M. M. Fateh, and M. R. Rafiei, "A robust anti-windup control design for electrically driven robots—theory and experiment," *International Journal of Control, Automation and Systems*, vol. 9, no. 5, pp. 1005–1012, 2011.
[24] B. J. Jonkman, "TurbSim user's guide: Version 1.50," National Renewable Energy Laboratory (NREL), CO, USA, Tech. Rep., 2009.
[25] F. Dunne, L. Y. Pao, D. Schlipf, and A. K. Scholbrock, "Importance of lidar measurement timing accuracy for wind turbine control," in *2014 American Control Conference*, OR, USA, Jun 2014, pp. 3716–3721.
[26] K. Z. Østergaard, J. Stoustrup, and P. Brath, "Linear parameter varying control of wind turbines covering both partial load and full load conditions," *International Journal of Robust and Nonlinear Control*, vol. 19, no. 1, pp. 92–116, 2009.
[27] G. Hayman, "MLife theory manual for version 1.00," National Renewable Energy Laboratory (NREL), CO, USA, Tech. Rep., 2012.